

---

# HIGH-RESOLUTION FLOOD PROBABILITY MAPPING USING GENERATIVE MACHINE LEARNING WITH LARGE-SCALE SYNTHETIC PRECIPITATION AND INUNDATION DATA

---

Lipai Huang<sup>a,\*</sup>, Federico Antolini<sup>b</sup>, Ali Mostafavi<sup>a,b</sup>, Russell Blessing<sup>b</sup>, Matthew Garcia<sup>c</sup>, Samuel D. Brody<sup>b</sup>

<sup>a</sup> Urban Resilience.AI Lab, Zachry Department of Civil and Environmental Engineering, Texas A&M University, College Station, TX

<sup>b</sup> Institute for a Disaster Resilient Texas, Texas A&M University, College Station, TX

<sup>c</sup> Civil and Environmental Engineering, Rice University, Houston, TX

\* corresponding author, email: lipai.huang@tamu.edu

## ABSTRACT

High-resolution flood probability maps are essential for addressing the limitations of existing flood risk assessment approaches but are often limited by the availability of historical event data. Also, producing simulated data needed for creating probabilistic flood maps using physics-based models involves significant computation and time effort inhibiting the feasibility. To address this gap, this study introduces *Flood-Precip GAN* (Flood-Precipitation Generative Adversarial Network), a novel methodology that leverages generative machine learning to simulate large-scale synthetic inundation data to produce probabilistic flood maps. With a focus on Harris County, Texas, *Flood-Precip GAN* begins with training a cell-wise depth estimator using a limited number of physics-based model-generated precipitation-flood events. This model, which emphasizes precipitation-based features, outperforms universal models. Subsequently, a Generative Adversarial Network (GAN) with constraints is employed to conditionally generate synthetic precipitation records. Strategic thresholds are established to filter these records, ensuring close alignment with true precipitation patterns. For each cell, synthetic events are smoothed using a K-nearest neighbors algorithm and processed through the depth estimator to derive synthetic depth distributions. By iterating this procedure and after generating 10,000 synthetic precipitation-flood events, we construct flood probability maps in various formats, considering different inundation depths. Validation through similarity and correlation metrics confirms the fidelity of the synthetic depth distributions relative to true data. *Flood-Precip GAN* provides a scalable solution for generating synthetic flood depth data needed to create high-resolution flood probability maps, significantly enhancing flood preparedness and mitigation efforts.

**Keywords** Flood Risk · Generative Modeling · Machine Learning · Synthetic Data · Data Augmentation · Precipitation Events Generation

## 1 Introduction

Flood hazards pose a significant threat to cities and communities globally, resulting in extensive physical damage and substantial economic costs due to material losses and human casualties, particularly in densely populated regions. In the United States, flood-related insurance claims have consistently averaged around \$40 billion annually over the past four decades [1]. With the projected increase in the frequency and severity of flood events across various U.S. regions [2, 3], this financial burden is expected not only to persist but also to escalate. The prompt and accurate assessment of flood risk is crucial for the efficient response and recovery of affected communities. Spatial flood risk characterization traditionally involves the creation of floodplain maps, which delineate areas typically prone to flooding based on historical data and hydrological models. These maps are crucial for flood risk reduction, urban planning, and development regulations, as they identify regions where flood risk management strategies are most needed. However, floodplain maps often possess limitations due to their reliance on limited historical data, which may not accurately reflect current conditions.

Also, development of floodplains using physics-based hydraulic and hydrologic (H&H) models is computationally expensive. In addition, these maps usually depict flood extent limited to a specific expected frequency of flooding, limiting their utility in risk assessments and communication. The gaps in traditional floodplain mapping underscore the need to incorporate probability into flood maps beyond the traditional 100-year and 500-year frequencies. In the context of this study, probabilistic flood maps quantify flood risk irrespective of the likelihood of rainfall events. That is, probabilistic flood maps estimate the likelihood that a rainfall event causes a certain inundation in a given place (e.g., 1 ft) from a large number of rainfall events, without considering the probability of occurrence of each of those. For example, if 350 out of 1000 rainfall events cause at least 1 ft inundation in a certain place, a probabilistic flood map will associate a likelihood of 0.35 to the 1-ft inundation of that place for rainfall events with the range of characteristics considered. This quantified likelihood provides a measure of 1-ft inundation risk in the area given the characteristics of rainfall events. In this context, this probability is different from the annual likelihood typically used which is based on the return period of rainfall events. By offering a probabilistic measure of flood risks (based on characteristics of rainfall events but independent of the return period of rainfall events), maps provide quantitative insights that help policymakers, planners, and communities to better prepare for and mitigate the impacts of potential flooding events with tailored, data-driven strategies. The creation of flood probability maps hinges on simulating a large number of flood inundation scenarios based on which the likelihood of a range of flood depths across a region can be estimated. In fact, one of the major barriers to creation of flood probability maps is the lack of numerous flood scenarios. On one hand, the limited number of historical flood events in a given region is not large enough to build a robust statistical distribution of rainfall events and their associated flood depths. Also, depending on the rate of land use change, historical data may not be adequate to estimate flood risk in current conditions. On the other hand, generating a large number of simulated flood scenarios using H&H models is computationally expensive and would not be feasible. An alternative to historical data is represented by synthetic high-resolution flood scenarios generated using generative models.

The use of generative models and machine learning has gained significant attention in flood risk analysis. Recent studies have adopted Generative Adversarial Networks (GANs) to improve data generation, such as [4], which uses GANs to generate synthetic precipitation data integrated with the Soil and Water Assessment Tool (SWAT) to enhance flood frequency analysis. Similarly, [5] employs machine learning models within a GAN framework for real-time flood forecasting in urban environments, improving prediction accuracy and emergency response strategies through event-based data modeling. Deep learning models, including Convolutional Neural Networks (CNNs) and Recurrent Neural Networks (RNNs), have been used for predicting flash flood probabilities and integrating with hydrodynamic models for efficient flood mapping and risk assessment [6]. Machine learning algorithms like Random Forest and Extreme Gradient Boosting (XGBoost) have been applied to assess flood susceptibility and generate flood risk maps by analyzing key flood conditioning factors [7, 8]. Furthermore, studies such as [9, 10] have developed ML-based models, including Long Short-Term Memory (LSTM) networks and conditional GANs, to enhance flood prediction accuracy in specific urban settings. Despite these advancements, there is currently no model for simulating synthetic flood data specifically for creating probabilistic flood maps. To address these challenges, we introduce *Flood-Precip GAN*, a novel methodology leveraging generative machine learning to synthesize large-scale inundation data. The main workflow is illustrated in Fig. 1. *Flood-Precip GAN* starts with the training of a depth estimator using a number of physics-based model-generated flood events, incorporating precipitation-based, spatial, and region-specific features. Following this, a Conditional GAN (CTGAN) with constraints is employed to generate synthetic rainfall precipitation events. Strategic thresholds are established to filter these synthetic records, ensuring close alignment with true precipitation patterns. For each location, synthetic events are smoothed using a K-nearest neighbors (KNN) algorithm and processed through the depth estimator to derive synthetic depth distributions. By iterating this procedure across multiple synthetic rainfall events, we construct flood probability maps for different rainfall categories with certain duration, maximum, and cumulative precipitation ranges. These maps are validated using similarity and correlation metrics to confirm the correspondence of synthetic depth distributions to true data. The novel contributions of the model presented in this paper are threefold:

- We introduce a novel methodology that utilizes a surrogate machine learning pipeline to estimate flood probabilities using synthetic precipitation-flood events generated by CTGAN.
- The cell-wise machine learning modeling, introduced in Section 2.3, presents an innovative approach to feature engineering, yielding enhanced prediction performance compared to global models.
- We develop an all-to-one event sampling algorithm designed to strategically improve the quality of synthetic records while preserving non-linearity, ensuring a more realistic simulation of flood events.

*Flood-Precip GAN* provides a scalable solution for generating high-resolution flood probability maps, significantly enhancing flood preparedness and mitigation efforts. The following section explains the components of the *Flood-Precip GAN* model and the associated datasets.

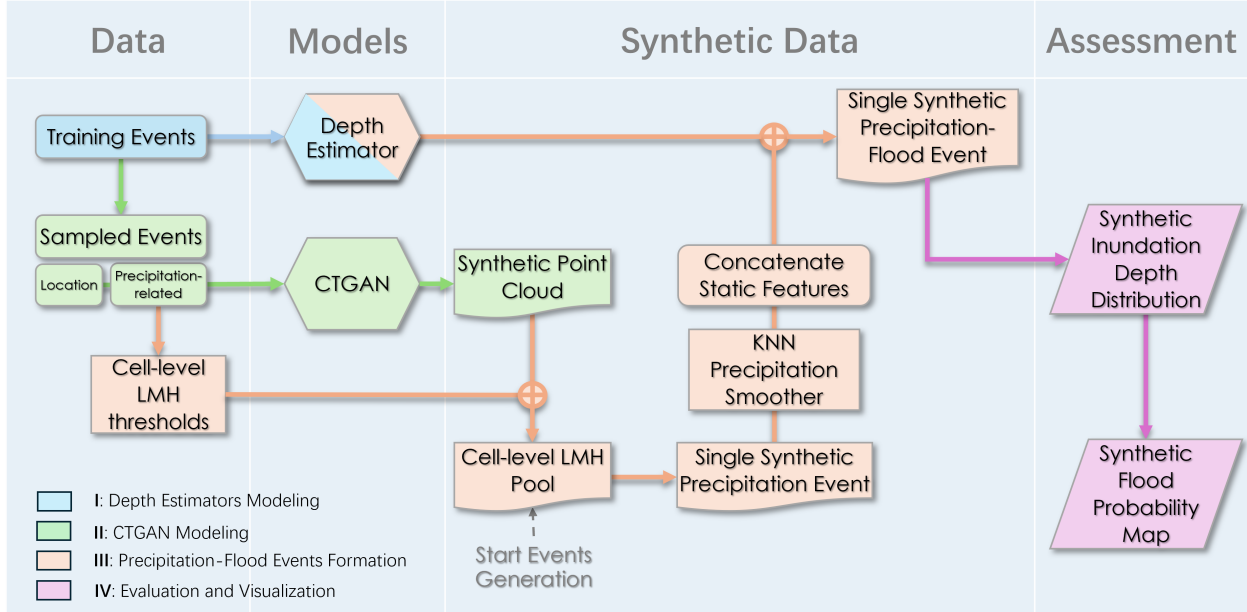


Figure 1: The main research workflow consists of four steps. **Step I** involves training and selecting the optimal model for depth estimation to generate synthetic depth data. **Step II** focuses on training a CTGAN with specific constraints and using conditional sampling to create a synthetic point cloud. In **Step III**, a cell-level LMH pool is developed based on thresholds derived from sampled training events, allowing for strategic sampling of features to produce synthetic precipitation-flood events with the depth estimator. Finally, **Step IV** repeats **III** to build a synthetic depth distribution, culminating in the creation of a synthetic flood probability map.

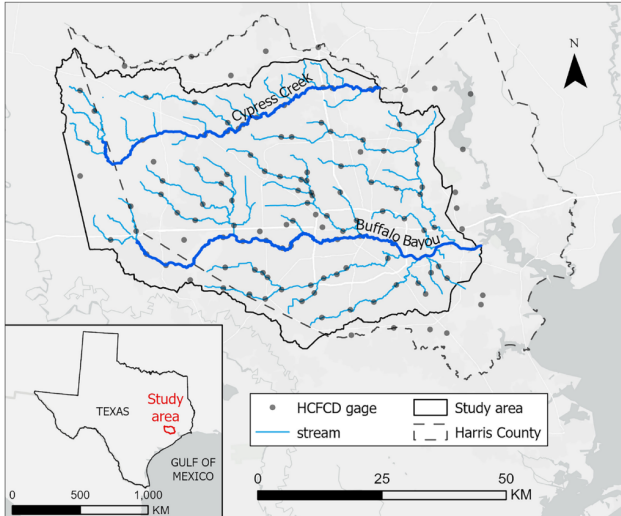


Figure 2: Study area and Harris County Flood Control District gauge distribution. Map created with *ArcGIS Pro 3.0.0* (<https://pro.arcgis.com/>).

## 2 Material and Methods

### 2.1 Study Region and Data

#### 2.1.1 Study Region

As Fig. 2 depicts, the test bed for creating the *Flood-Precip GAN* model is Harris County in Texas. The main watersheds are Cypress Creek and Buffalo Bayou. Harris County, the core county of the Greater Houston Metropolitan Statistical Area, spans 1,778 square miles (4,605 square kilometers) and has grown to over 4.5 million residents in the past decade. The county's flat topography, with elevations ranging from -40 ft (-12.19 meters) to 300 ft (91.44 meters), and predominantly developed land (over two-thirds), along with 20% pasture and cultivated lands [11], contribute to its flood risk. The Cypress Creek watershed in the north and the Buffalo Bayou system in the central and southern parts flow into

the San Jacinto River and the Ship Channel, eventually reaching the Gulf of Mexico. The area's dense development, poor natural drainage, limited soil infiltration, and subtropical climate significantly heighten its susceptibility to chronic flooding.

### 2.1.2 Data

In creating *Flood-Precip GAN*, there is a need for data related to flood inundation scenarios from a range of rainfall events. The lack of sufficient historical inundation data was addressed using 592 precipitation-flood events simulated by the HEC-RAS 2D model, a hydrologic software developed by the United States Army Corps of Engineers. This method, leveraging the advantages of the Rasterized Time-series Resampling Method (RTRM), is a non-denationalized bootstrapping approach for Radar Rainfall data that enhances input space coverage, captures spatiotemporal patterns, supports both temporal and spatial scaling, maintains the integrity of input dataset patterns, and facilitates interpolation to fill data gaps, providing smoother and more accurate coverage for hydrological modeling. The study area was modeled using a 1,200 ft  $\times$  1,200 ft (approximately 366 m) mesh grid, which was further refined along major watercourses and tributaries to improve computational stability and accuracy. The resulting mesh comprised 26,301 cells, providing a detailed representation of the area. Parameters such as Manning's roughness and imperviousness were derived from the 2019 National Land Cover Dataset [11], while soil infiltration values were sourced from the Gridded Soil Survey Geographic database [12]. Model validation involved analyzing data from Harris County Flood Control District gauges [13] during five significant flood events from 2016 to 2020, including the 2016 Tax Day flood and Hurricane Harvey in 2017. This validation process, which calibrated the HEC-RAS 2D model for global minimum error across all gauges, confirmed the model's reliability and accuracy for simulating diverse flood scenarios [14]. The rainfall events used in generating flood scenarios by HEC-RAS 2D are further used to generate synthetic rainfall events as described in the following sections. The generated flood depth scenarios were used to create the depth estimator (a surrogate machine learning model for determining maximum flood depth) given rainfall and other landscape features.

### 2.2 Preprocessing

We employed Voronoi tessellation [15] to partition the training dataset, assigning each point within the study area a unique polygonal region to ensure there is no overlap between cells. Additionally, we segmented the 592 rainfall events used in the HEC-RAS 2D flood scenarios into three inundation depth levels to ensure consistent stratification for subsequent dataset splitting and resampling. Specifically, for the training set, events are distributed with mean depths of  $\leq 2$  inches, between  $> 2$  and  $\leq 6$  inches, and  $> 6$  inches in a ratio of 2:4:1, respectively. The validation set consists of 20% of the training set volume, with the remaining data designated as the test set. This approach optimizes the separation of events to ensure relatively balanced representation across the training, validation, and testing phases, facilitating more effective modeling.

### 2.3 Depth Estimator Model

For the depth estimator component of *Flood-Precip GAN*, we chose a tree-based machine learning model trained on simulated scenarios from the HEC-RAS 2D model. Compared to traditional machine learning models, tree-based models have shown superior performance due to their ability to manage complex, non-linear relationships and interactions within the data. XGBoost [16, 17], in particular, excels with its gradient boosting framework, which iteratively improves model accuracy by minimizing residual errors from previous iterations. Additionally, deep learning models in regression, such as the Transformer [18, 19], utilize attention mechanisms to capture long-range dependencies and complex feature interactions, providing substantial benefits in predictive performance. In this study, we employed the XGBoost regressor and the regression transformer as universal depth estimators, training them on physics-based model-generated events that include both spatial features incorporating channel presence and terrain elevation, and precipitation-based features as shown in Table 1. This integration aims to enhance the accuracy and robustness of maximum flood inundation estimations. Furthermore, we compared these universal models with a cell-wise model, MaxFloodCast V2 [20], an XGBoost-based depth estimator trained specifically on individual cell meshes, resulting in 26,301 models corresponding to the 26,301 cells. Due to the unique nature of cell-wise model implementation, we assumed geospatial changes to be negligible across all events, thereby excluding spatial features. To account for the influence of inter-watershed precipitation without directly utilizing static geospatial features, we introduced cumulative and peak precipitation ratios as shown in Eq. 1 and Eq. 2 to effectively capture interactions among watersheds.

$$\text{Heavy Peak (Cumulative) Precipitation Ratio}_i = \frac{\sum_j AC_{i,j} \times h_{i,j}}{AW_i} \quad (1)$$

$$h_{i,j} = \begin{cases} 1, & \text{if } p_{i,j} > 2 \text{ in,} \\ 0, & \text{otherwise.} \end{cases} \quad (2)$$

where  $AW_i$  represents the area of watershed  $i$ ,  $AC_{i,j}$  represents the area of cell  $j$  in watershed  $i$ ,  $h_{i,j}$  is a binary identifier of cell  $j$  in watershed  $i$ , and  $p_{i,j}$  denotes the peak (cumulative) precipitation in cell  $j$  within watershed  $i$ .

Heavy peak precipitation ratio and heavy cumulative precipitation ratio are defined at the watershed level and thus are constant across all cells of a watershed for a given rainfall event. These two ratios can vary significantly across different events and watershed regions, providing substantial explanatory potential.

Table 1: Features used in Depth Estimator.

Feature	Level	Unit	Description
Cumulative Precipitation	All	Inch	Event total precipitation
Peak Precipitation	All	Inch	Event peak precipitation
Duration	All	Hour	Effective precipitation duration
Channel	Universal	Binary (1 or 0)	Identification of channel cell
Terrain Elevation	Universal	Feet	Geographical height of each cell
9 Heavy Cumulative Precipitation Ratio (one for each watershed)	Cell-wise	Scalar (range 0 to 1)	Proportion of watershed area experiencing heavy cumulative precipitation
9 Heavy Peak Precipitation Ratio (one for each watershed)	Cell-wise	Scalar (range 0 to 1)	Proportion of watershed area experiencing heavy peak precipitation

We assessed the predictive performance of the depth estimators (in Section 3.1) using Root Mean Squared Error (RMSE) and R-squared ( $R^2$ ) scores [21] to evaluate both accuracy and explainability. RMSE measures the average magnitude of the prediction errors, providing insight into the estimator's precision, while  $R^2$  indicates the proportion of variance in the observed data that is predictable from the input features, reflecting the model's explanatory power. In addition, we conducted a comprehensive analysis of the aggregated performance of these models on both channel and non-channel cells. This distinction is crucial due to the varying hydrological and ground texture characteristics inherent to these environments, which influence the uncertainty and behavior of flood dynamics.

## 2.4 Rainfall Data Augmentation via CTGAN

The rainfall events considered in simulating flood scenarios with the physics-based model were limited to 592 events. To increase the number of rainfall events and generate synthetic rainfall events in our study, we employed Conditional Generative Adversarial Networks (CTGAN) from SDV [22, 23] for tabular data augmentation. CTGAN extends the GAN framework to handle structured data, particularly tabular datasets, making it highly effective for generating synthetic data in scenarios with small, imbalanced datasets. One of CTGAN's strengths is its ability to support the specification of constraints and conditions during the data generation process, enabling the preservation of specific relationships or attributes present in the original dataset.

We converted the true cell-level data into point-level data using centroids to facilitate generation. Consequently, the input attributes for CTGAN included latitude, longitude, cumulative precipitation, peak precipitation, and duration. To enhance the quality of the synthetic records, we introduced several constraints to ensure the synthetic point data adhered to the following conditions: (1) the data remained within specified geographical boundaries, (2) the cumulative precipitation exceeded the peak precipitation, and (3) the peak precipitation surpassed the unit precipitation, calculated by dividing the cumulative precipitation by the duration.

To determine the optimal hyperparameters for the generator and discriminator learning rates, as well as the stoppage epochs, we conducted a comprehensive hyperparameter grid search. The grid search was crucial due to the complexity of balancing the learning rates for the generator and discriminator, ensuring both networks improved steadily without overpowering each other. Additionally, selecting appropriate stoppage epochs enabled us to terminate the training process at the most accurate point, preventing overfitting or underfitting. The optimal checkpoint was selected based on the corresponding synthetic dataset achieving the highest average marginal distribution, as evaluated using the Kolmogorov-Smirnov statistic (KS statistic) [24]. The KS statistic  $K$  for a particular feature  $x_i$  between the training dataset and the synthetic dataset is defined as follows:

$$K_{i,n,m} = \sup_{x_i} |F_{t,n}(x_i) - F_{s,m}(x_i)| \quad (3)$$

Where  $F_{t,n}$  and  $F_{s,m}$  represent the empirical distribution functions of the training dataset and the synthetic dataset generated by CTGAN, respectively. The function  $\sup_{x_i}$  denotes the supremum across the domain of feature  $x_i$ . The overall quality score for all features, excluding location-based features, in the synthetic dataset is computed using the following formula:

$$Score = \frac{\sum_{i=1}^N (1 - K_{i,n,m})}{N} \quad (4)$$

Where  $N$  is the number of features. A higher score indicates a higher quality of the synthetic data, signifying a closer approximation to the true data distribution. The outcome of this step is a comprehensive synthetic point cloud containing

10,000,000 synthetic rainfall records generated by CTGAN, representing various precipitation durations. This diverse point cloud presents a significant challenge in processing and formulating individual precipitation events under varying conditions.

## 2.5 Rainfall Events Generation

In the synthetic point dataset, which comprises collections of precipitation records, we have predefined thresholds for cumulative precipitation, peak precipitation, and duration—categorized as Low, Medium, and High (LMH)—for each cell mesh. These categories are established based on the following conditions:

Table 2: Definition of LMH Thresholds for Each Precipitation-Based Feature within a Cell Mesh.

Class	Range
Low	$[0, \mu_i - \theta_1 \cdot \sigma_i]$
Medium	$(\mu_i - \theta_1 \cdot \sigma_i, \mu_i + \theta_2 \cdot \sigma_i]$
High	$(\mu_i + \theta_2 \cdot \sigma_i, +\infty)$

Where  $\mu_i$  is the mean of a precipitation-based feature  $x_i$  from training dataset, and  $\sigma_i$  refers to its standard deviation.  $\theta_1$  and  $\theta_2$  are two positive constants. Consequently, for each cell mesh, we established low (L), medium (M), and high (H) thresholds based on the distribution of precipitation-based features (cumulative precipitation, peak precipitation and duration) from the training dataset. These thresholds were then applied to the synthetic point dataset generated as described in section 2.4. We conducted a comprehensive iteration over all synthetic point records, retaining the index of a point record to corresponding cell-level feature pool only if all its synthetic precipitation-based features consistently matched within the same LMH classification. This rigorous iterative screening ensured that each cell’s pool included indices of synthetic records that not only covered a range of precipitation levels but also met stringent quality criteria.

With the establishment of the synthetic indices pool for each cell, we were enabled to generate global precipitation events across the study area. For each event generation, a specific duration was sampled randomly from the aggregated pool to set as the global rainfall duration, constraining the potential pool. Subsequently, each cell randomly sampled a synthetic record from its tailored pool to represent the entire cell mesh. In instances where some cells returned an empty record, we employed a K-Nearest Neighbors (KNN) approach [25] to generate records by averaging the attributes of surrounding neighbors, effectively filling any gaps. This strategic sampling allowed us to create isolated synthetic precipitation events from a large point cloud, transitioning from point-level to cell-level representation. To enhance the approximation of true precipitation events, we applied the KNN method as a smoother [26] to both cumulative and peak precipitation data. Additionally, we computed heavy precipitation ratios from these smoothed values to highlight interactions among various watersheds. Following this cell-level processing, we utilized the depth estimator with optimal predictive performance as identified in Section 2.3 to generate inundation depths from the aggregated synthetic features, thus completing the precipitation-flood event. After thousands of iterations of individual rainfall event generation, we built synthetic inundation depth distribution for each cell, enabling the estimation of the frequency of rainfall events that cause certain flood depth levels in different areas in producing the synthetic flood probability maps.

To rigorously assess the event-generation performance, we evaluated the statistical similarity between the true inundation depth distribution and the synthetic inundation depth distribution. We implemented interpolation using the formula in Eq. 5 for the synthetic depth distribution  $\mathbf{d}_s$  to ensure the same dimension as the training depth distribution  $\mathbf{d}_t$ , facilitating the evaluation. Let  $\mathbf{d}_t = [d_t(1), d_t(2), \dots, d_t(m)]$  be the training depth vector with  $m$  records, and  $\mathbf{d}_s = [d_s(1), d_s(2), \dots, d_s(n)]$  be the synthetic depth vector with  $n$  synthetic records. We define an interpolation function  $f$  such that:

$$f(i) = d_s(i) \quad \text{for } i = 1, 2, \dots, n$$

The interpolated values  $d'_s(j)$  for  $j = 1, 2, \dots, m$  are given by:

$$d'_s(j) = f\left(\frac{j-1}{m-1} \cdot (n-1) + 1\right) \quad (5)$$

This process ensures that  $\mathbf{d}_t$  and  $\mathbf{d}'_s$  are of the same length, enabling valid comparisons using multiple statistical measures. Cosine similarity [27] assesses their directional similarity, Pearson correlation [28] evaluates the linear relationship between the two distributions, and Kullback-Leibler (KL) divergence [29] quantifies how one probability

distribution diverges from the other. The corresponding formula is shown below:

$$\text{Cosine Similarity}(\mathbf{d}_t, \mathbf{d}'_s) = \frac{\mathbf{d}_t \cdot \mathbf{d}'_s}{\|\mathbf{d}_t\| \|\mathbf{d}'_s\|} \quad (6)$$

$$\text{Correlation}(\mathbf{d}_t, \mathbf{d}'_s) = \frac{\sum_{i=1}^m (d_t(i) - \bar{d}_t)(d'_s(i) - \bar{d}'_s)}{\sqrt{\sum_{i=1}^m (d_t(i) - \bar{d}_t)^2 \sum_{i=1}^m (d'_s(i) - \bar{d}'_s)^2}} \quad (7)$$

$$D_{KL}(\mathbf{p} \parallel \mathbf{q}) = \sum_{i=1}^m p(i) \log \frac{p(i)}{q(i)}, \quad p(i) = \frac{d_t(i)}{\sum_{k=1}^m d_t(k)}, \quad q(i) = \frac{d'_s(i)}{\sum_{k=1}^m d'_s(k)} \quad (8)$$

where  $\mathbf{p}$  and  $\mathbf{q}$  are the normalized versions of  $\mathbf{d}_t$  and  $\mathbf{d}'_s$ , respectively. Besides the averaged synthetic depth distribution across the study region, we further explore the performance by aggregating the results into channel and non-channel levels, as described in Section 2.3. This detailed analysis allows us to assess how well the synthetic data captures the unique characteristics of different regions in the study area.

### 3 Results

#### 3.1 Selection of Depth Estimator

To understand the advancements of tree-based models and transformers in regression problems, specifically in the context of inundation depth estimation, we compared the predictive performance of two universal models, XGBoost Regressor and Regression Transformer, with one cell-wise model, MaxFloodCast V2. MaxFloodCast V2 utilizes an XGBoost-based architecture and incorporates heavy precipitation ratio features. We trained the Regression Transformer, configured with 4 layers in the Transformer encoder, a dimensionality of 128, 2,048 in the feed-forward layer, and 8 attention heads with 25% dropout, on 8 NVIDIA RTX A100 GPUs. The XGBoost Regressor was trained on an NVIDIA RTX A6000, while MaxFloodCast V2 was trained in parallel on an AMD EPYC 7702P 64-Core Processor, sharing the same hyperparameter settings as the XGBoost Regressor. The objective function minimized squared errors with a learning rate of 0.01. The XGBoost model built 1000 trees with a maximum depth of 5, incorporating L1 regularization to prevent overfitting and a subsample ratio of 0.3 to introduce non-linearity and enhance robustness. Following the sampling strategy mentioned in Section 2.2, we configured 252 true precipitation-flood events for training, 63 events for validation, and the remaining events as the test set. The comparison results are presented in Table 3, which assesses the overall, channel, and non-channel RMSE, as well as the  $R^2$  score. The resulted comparison reveals significant

Table 3: Depth Estimator Comparison on true test dataset.

Model	Level	Overall RMSE	Overall $R^2$	Channel RMSE	Channel $R^2$	Non-channel RMSE	Non-channel $R^2$
Regression Transformer[18]	Universal	2.6634	0.6537	4.1264	0.7278	2.4133	0.4928
XGBoost Regressor[16]	Universal	2.6916	0.6463	4.2755	0.7078	2.4153	0.4920
MaxFloodCast V2[20]	Cell-wise	0.6996	0.9189	1.7280	0.9107	0.5680	0.9200

differences in the predictive performance between the universal models and the cell-wise model. The Regression Transformer and XGBoost Regressor both show substantial errors, with overall RMSE scores above 2 ft, indicating they struggle to accurately predict inundation depths. Their performance is particularly poor in channel cells, where RMSE values exceed 4 ft. In contrast, MaxFloodCast V2 demonstrates superior performance with an overall RMSE of 0.6996 ft and an  $R^2$  value of 0.9189, significantly outperforming the universal models. It achieves lower RMSE in both channel (1.7280 ft) and non-channel cells (0.5680 ft), highlighting its accuracy and reliability. The cell-wise approach of MaxFloodCast V2, which tailors the model to the specific characteristics of each cell, allows it to better capture local variations in precipitation and terrain features, resulting in more accurate predictions. Also, the incorporation of heavy precipitation ratio features enhances its ability to represent interactions between watersheds. The dataset used for training, generated by the physics-based model, is both limited and imbalanced, comprising 90 true events. This limitation affects the universal models more significantly, as they are less adept at handling such imbalances compared to the specialized cell-wise approach of MaxFloodCast V2. Overall, the results highlight the effectiveness of the cell-wise approach in flood depth estimation, particularly in regions with complex hydrological dynamics, making MaxFloodCast V2 the optimal depth estimator for the *Flood-Precip GAN* model.

#### 3.2 CTGAN-generated Precipitation Records Quality Review

We strategically sampled 90 true events following the ratio described in Section 2.2 and configured 36 hyperparameter sets for our grid search. This involved combining six pairs of learning rate settings with six distinct stoppage epochs,

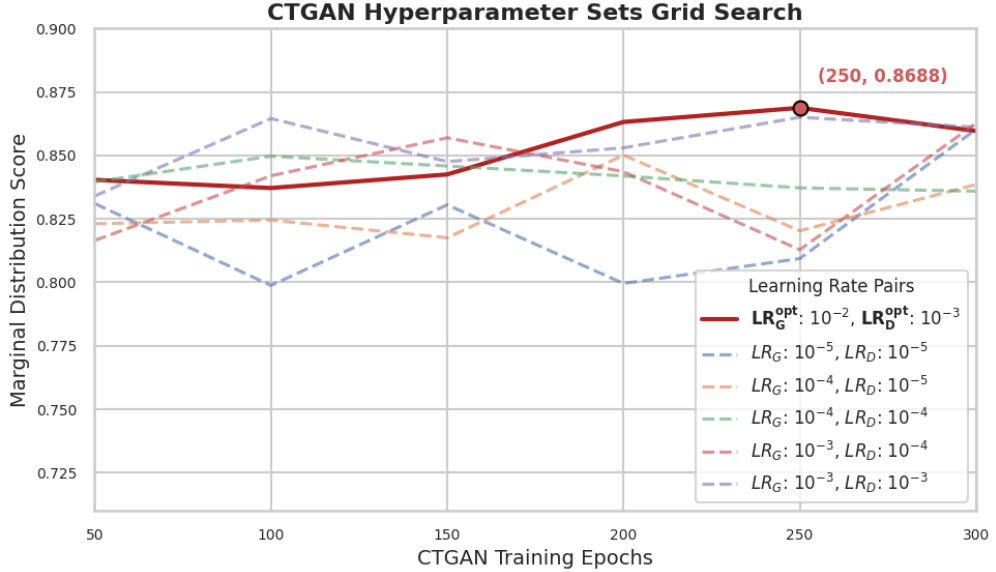


Figure 3: Grid search results for CTGAN hyperparameters. The optimal hyperparameter set was selected based on the highest average marginal distribution scores across all synthetic precipitation-based features generated by the best-performing CTGAN configurations. The key hyperparameters explored in the grid search include the generator and discriminator learning rates, as well as the number of training epochs.

increasing from 50 epochs to 300 epochs in increments of 50, and modeling on NVIDIA’s RTX A6000 GPU. This meticulous grid search focused on generating records under the condition duration  $\geq 1$ , targeting the potential simulation of global precipitation events. As shown in Fig. 3, we identified the optimal checkpoint with a generator learning rate of  $10^{-2}$ , a discriminator learning rate of  $10^{-3}$ , and early stopping at 250 epochs. Notably, the generator learning rate is set to be 10 times higher than that of the discriminator to prevent the generator from being overpowered in the early stages before it can effectively learn the underlying data patterns. Ultimately, both the generator and discriminator converged before reaching the 300-epoch limit. The optimal settings enabled a direct comparison of cumulative precipitation, peak precipitation, and duration between the training dataset and the 10,000,000 synthetic data points generated by CTGAN, as depicted in Fig. 4. This configuration produced an average marginal distribution score of 0.802, demonstrating a high fidelity of the synthetic data, particularly for cumulative and peak precipitation when compared to the original dataset. As shown in Fig. 4(c), we enforced a constraint in CTGAN that limits duration  $\leq 1$ , since our focus is primarily on global precipitation event generation. Additionally, the CTGAN model maintains the flexibility to generate local precipitation events by allowing cumulative precipitation to drop to zero. Moving forward, the challenge remains to construct isolated precipitation-depth events from the synthetic point dataset that closely correlate with true events, thus advancing the goals of this research in generating probabilistic flood maps.

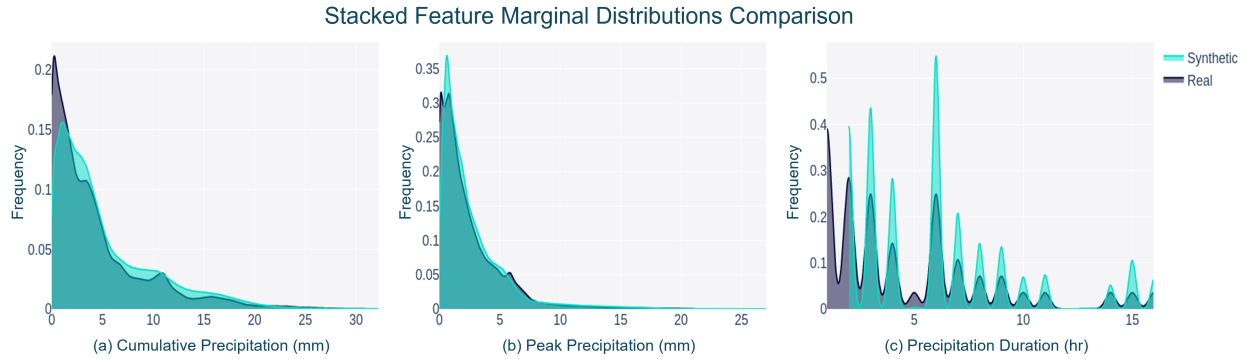


Figure 4: Stacked Marginal Distribution Comparison of Three Synthetic Features between training data and synthetic data: (a) cumulative precipitation, (b) peak precipitation and (c) duration. The distribution of the training dataset is represented in gray, while the synthetic distribution is depicted in light blue. Distributions were generated using the Synthetic Data Vault (SDV) [22].

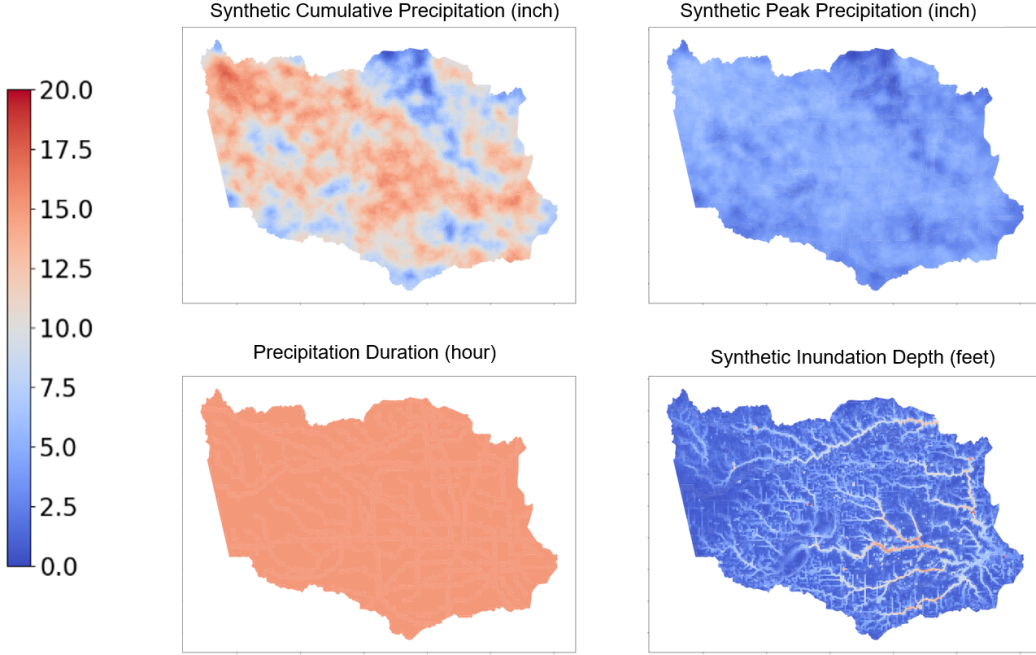


Figure 5: Synthetic flood event with 15 hours global precipitation. The synthetic cumulative precipitation and peak precipitation are processed by 50-NN smoother. Maps generated by *Geopandas* Python package.

### 3.3 Synthetic Rainfall Event Assessment

Using the strategic filtering and sampling methods introduced in Section 2.5, we generated 10,000 rainfall events through parallel computing. For each event, the global duration was sampled from the tailored pool. As the number of event simulations increases, the overall synthetic precipitation events tend to closely resemble true events. We used 20-nearest neighbors (20-NN) to fill the empty cells after stringent filtering, using averaged precipitation-based feature values. It is common to observe a pepper-salt appearance in cumulative and peak precipitation maps due to the independence of point data in CTGAN records generation. To address this, we applied 20-NN smoothing for synthetic precipitation events with duration of 2 hours or less, and 50-NN smoothing for longer duration, to enhance the realism of the synthetic events. From these smoothed cumulative and peak precipitation features, we derived heavy cumulative and peak precipitation ratios, resulting in 21 input features for the selected depth estimator, MaxFloodCast V2, to generate synthetic inundation depths and complete the precipitation-flood event. The event generation process took an average of 10 minutes to generate 100 rainfall events in parallel, consuming 100 GB of memory on an AMD EPYC 7702P 64-core processor.

Fig. 5 illustrates a synthetic precipitation-flood event with a global duration of 15 hours, comprising four subplots: synthetic cumulative precipitation, synthetic peak precipitation, precipitation duration, and synthetic inundation depth. The cumulative and peak precipitation maps show significant spatial variability, with higher values in central and northern regions. Despite setting a global duration of 15 hours, the method effectively creates localized precipitation patterns. The inundation depth map highlights flood-prone regions, particularly along river channels and low-lying areas. This synthetic event realistically represents potential flood scenarios, enhancing flood risk assessment and mitigation efforts.

We generated 10,000 synthetic precipitation-flood events, providing each cell with a comprehensive synthetic depth distribution for direct comparison with the training dataset. To assess the performance of the synthetic events, we utilized four key metrics—RMSE, Cosine Similarity, Correlation, and KL Divergence—comparing them against the limited number of sampled training events. To ensure a fair comparison, the synthetic events were downsampled to match the size of the training data. This downsampling process was repeated 50 times to minimize variability introduced by randomness. A detailed statistical comparison between the normalized versions of the training and synthetic datasets is provided in Table 4, with the corresponding visualizations shown in Fig. 6.

The synthetic data demonstrates strong overall performance, as evidenced by the RMSE and cosine similarity metrics, indicating that the generated events align closely with the training data and accurately capture key hydrological characteristics and trends. Notably, the mean RMSE for non-channel cells is 2.12 ft, substantially lower than the 5.96 ft recorded for channel cells. This disparity suggests that the synthetic data more effectively represents regions with

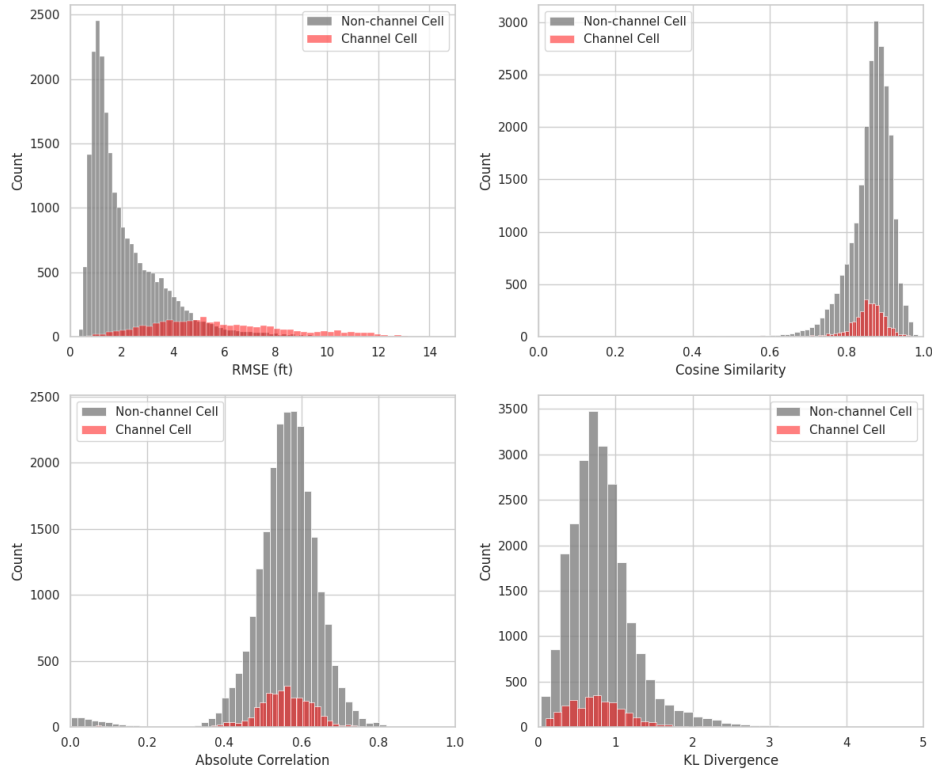


Figure 6: Comparison of Sampled Training Depth Distribution with Downsampled Synthetic Depth Distribution.

simpler hydrodynamics, while the higher RMSE in channel cells reflects the inherent difficulty in modeling real-world depth distributions in areas characterized by dynamic flow patterns and greater variability. Nevertheless, the synthetic data performs well even in these more complex regions, achieving a mean cosine similarity of 0.85 for channel cells, highlighting the model’s ability to capture the overall structure and trends of the real data.

In non-channel cells, the model excels with a mean cosine similarity of 0.86 and a relatively low KL divergence of 0.83. These metrics suggest that the synthetic data closely matches the probability distributions of the real data in these regions, where simpler hydrological behavior makes depth distributions easier to replicate. In contrast, the KL divergence for channel cells, though still low at 0.80, indicates some deviation between the synthetic and real data, which is expected given the complexity and variability of flood behavior in these more dynamic areas.

The correlation between the synthetic and real datasets further reinforces the model’s effectiveness. Non-channel cells exhibit a mean correlation of 0.56, while channel cells show a slightly lower but still robust correlation of 0.55. This highlights the model’s ability to capture linear relationships across both cell types, though the more intricate hydrodynamic processes in channel cells present additional challenges. Hydrologically, these findings are particularly significant. Channel cells, which are more prone to flooding due to their dynamic flow patterns, underscore the model’s strength in capturing intricate interactions even under complex conditions. The model’s ability to generalize across non-channel cells, reflected in their lower RMSE and KL divergence values, is equally noteworthy. It demonstrates the model’s capacity to explore a variety of flood scenarios without overfitting to specific events.

Geographically, the clear distinction between channel and non-channel cells emphasizes the importance of local topographical and hydrological features in flood modeling. The synthetic data performs particularly well in regions with less complex hydrodynamics, while still maintaining a reasonable alignment in more intricate areas.

Overall, these results highlight the strong potential of the synthetic dataset for reliable flood depth estimation across diverse regions, especially in flood-prone channel areas where accurate modeling is crucial for effective risk assessment and mitigation. The close alignment between the synthetic and training data across multiple metrics underscores the robustness of the approach, demonstrating its ability to replicate complex flood patterns while maintaining generalizability across varied hydrological landscapes. These findings affirm the method’s suitability for predictive flood modeling and underscore its potential as a powerful tool for future flood risk assessment and management efforts.

Building on this analysis, we generated flood probability maps. Fig. 7 presents synthetic flood probability maps for various inundation depths: 1 ft, 2 ft, 4 ft, and 6 ft. These maps highlight the probability of exceeding specified flood

Table 4: Statistical comparison of sampled training depth distribution and downsampled synthetic depth distribution for key metrics across Overall, Channel, and Non-channel Cells.

Metric	RMSE (ft)	Cosine Similarity	Correlation	KL Divergence
<b>Overall</b>				
Count	26301	26301	26301	26301
Mean	2.5527	0.8624	0.5567	0.8246
Std	2.0734	0.0549	0.0982	0.4566
Min	0.3184	0.3448	0.0010	0.0231
25%	1.1368	0.8389	0.5182	0.5365
50%	1.7974	0.8714	0.5651	0.7607
75%	3.3121	0.8976	0.6109	1.0103
Max	26.765	0.9861	0.8923	6.2082
<b>Channel</b>				
Count	2985	2985	2985	2985
Mean	5.9555	0.8545	0.5481	0.7980
Std	2.7691	0.0497	0.0981	0.4488
Min	0.5995	0.4680	0.0015	0.0918
25%	3.9065	0.8349	0.5126	0.4762
50%	5.4270	0.8600	0.5567	0.7506
75%	7.6582	0.8833	0.6045	1.0080
Max	26.765	0.9648	0.7927	5.2297
<b>Non-channel</b>				
Count	23316	23316	23316	23316
Mean	2.1171	0.8634	0.5578	0.8280
Std	1.4817	0.0554	0.0981	0.4575
Min	0.3184	0.3448	0.0010	0.0231
25%	1.0865	0.8398	0.5193	0.5430
50%	1.5940	0.8730	0.5663	0.7616
75%	2.7402	0.8993	0.6115	1.0106
Max	16.850	0.9861	0.8923	6.2082

depths across the study area. The probability values specify the proportion of precipitation-flood events that cause flood depths of certain level or higher in a given area across the 10,000 precipitation-flood events. These values capture the flood risk of certain areas for certain inundation levels. A high  $P(\text{depth} \geq 6 \text{ ft})$  in a given area means that for a generated generic flood event there is a high probability that flood level will equal or exceed 6 ft. In other words, the probability value serves as a quantification of risk to a certain depth of flooding. This interpretation should be distinct from annual flood probability which is used in standard flood mapping methods. As shown in Fig. 7, at 1 ft and 2 ft depths, flood probabilities greater than 0.5 (high probability) are predominantly observed in the northeastern, southeastern, and central regions of the study area, while lower probabilities are seen in the western and southern areas. As the depth threshold increases to 4 ft and 6 ft, the high-probability zones become more concentrated along rivers/channels and low-lying regions, while most of the area shows low flood risk.

## 4 Discussion

In this study, we presented an innovative methodology, *Flood-Precip GAN*, for generating high-resolution flood probability maps using synthetic precipitation-flood events. Our approach leveraged advanced machine learning techniques, including Conditional Generative Adversarial Networks (CTGAN) [23] as point location and precipitation-based features generator and XGBoost-based models MaxFloodCast [20] as synthetic depth estimator, to overcome the limitations of traditional flood modeling that rely heavily on historical data. To address the limitations in feature dimensionality found in existing CTGAN tools and the challenge of generating individual precipitation-flood events from a massive synthetic point cloud, we designed a robust and systematic workflow. This approach includes cell-level pool creation, strategic sampling, noise smoothing, depth synthesis, and the eventual formation of individual events. Each step in the process is carefully structured to avoid overfitting and ensure that the generated synthetic events accurately reflect real-world flood scenarios while maintaining computational efficiency and high fidelity to hydrological patterns. By generating 10,000 synthetic precipitation-flood events, we created a comprehensive dataset that captures a wide spectrum of potential flood scenarios, significantly improving the robustness of flood risk assessments. Based on the metrics between the training and synthetic events across overall, channel, and non-channel aspects shown on Table 4, the overall Cosine Similarity, with a mean of 0.86 and a standard deviation of 0.05, indicates a strong alignment between the synthetic and training data. The RMSE values highlight a notable difference between channel and non-channel cells, reflecting the challenges in accurately modeling flood depth distribution in regions with dynamic flows and greater variability. These findings demonstrate the model's ability to capture key trends and linear relationships, particularly in hydrologically complex regions such as channel cells, which are more susceptible to flooding. Additionally, the synthetic data's capacity to generalize beyond the training events highlights its potential for producing realistic flood simulations, which is critical for accurate risk assessment and effective mitigation planning.

The flood probability maps provide an in-depth spatial analysis of flood risk, revealing critical high-risk zones, particularly along river channels and low-lying areas. These maps emphasize the importance of depth-specific flood

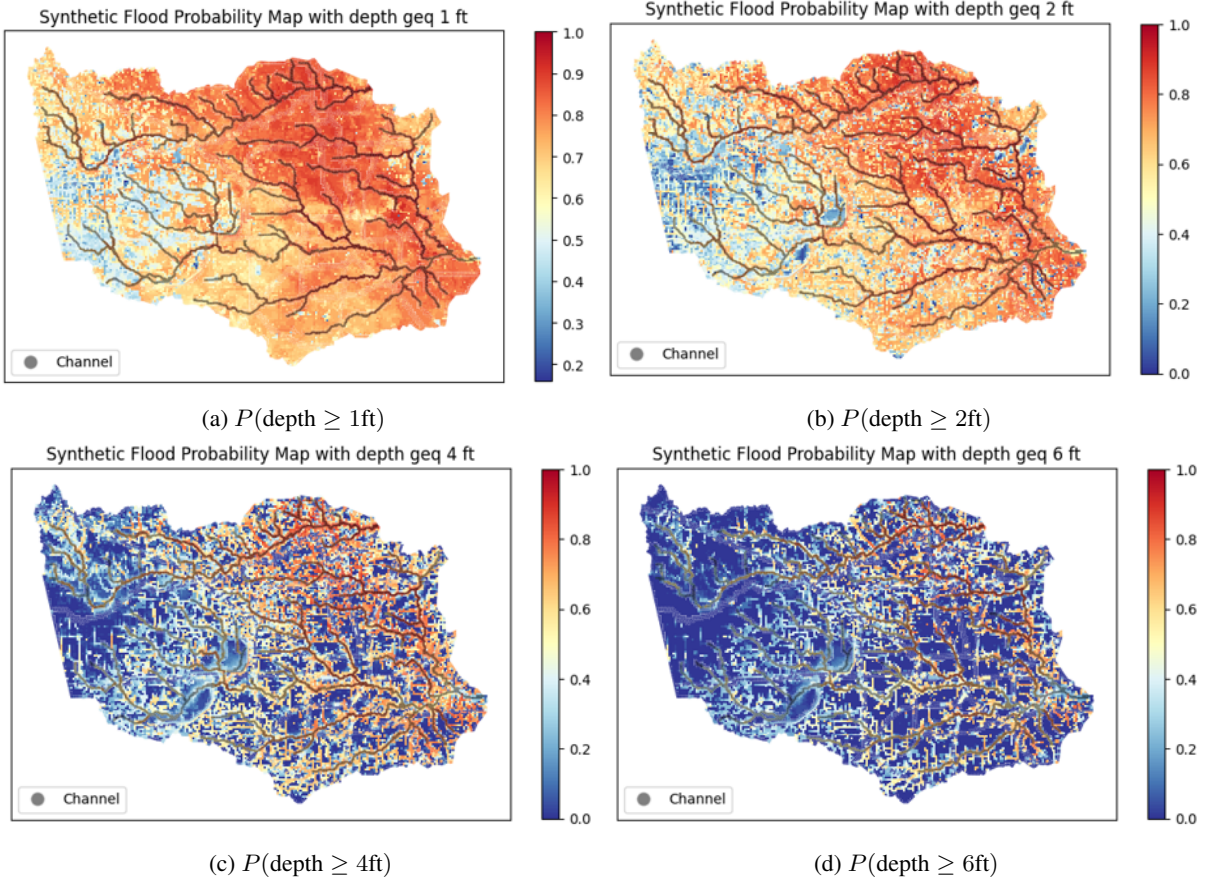


Figure 7: Synthetic flood probability maps based on four inundation depth criteria. The color gradient from blue to red represents probabilities ranging from 0 to 1 for a global precipitation event, with blue indicating lower probabilities and red indicating higher probabilities. Channel cells are highlighted in gray. Maps generated by *Geopandas* Python package.

management strategies, as the distinction between channel and non-channel cells highlights the need to account for topographical and hydrological variability. This is particularly crucial in regions where intricate flow dynamics, terrain elevation, and slope significantly influence flood behavior. The high resolution of the maps also allows for practical applications, such as assessing the flood risk of buildings by integrating lowest floor elevation datasets, identifying structures at risk of inundation over 2 ft. Additionally, these maps can evaluate transportation network vulnerability, as roads in areas with a high probability of exceeding 2 ft of inundation would become impassable, disrupting transportation and emergency response efforts. The non-binary nature of the maps further allows for comparative flood risk assessments across different inundation levels, enabling more nuanced and targeted flood mitigation strategies across diverse landscapes.

Moreover, the synthetic dataset's ability to simulate a broad range of generic flood scenarios, combined with its strong alignment to the training data, reinforces its applicability for future flood risk assessments. These findings suggest that this approach could play a pivotal role in enhancing predictive capabilities for flood events, enabling more effective planning and resource allocation for flood management in both simple and hydrologically complex regions.

Despite these advancements and novelties, the current approach has limitations in generating local precipitation events, even if the synthesizer has capability to generate records with no precipitation under a global precipitation duration. Plus, the computational complexity is significant, taking approximately 10 minutes and 100GB CPU memory to generate 100 precipitation-flood events. Future work should focus on improving the efficiency of the computational process and enhancing the model's ability to generate more localized precipitation patterns.

Overall, this study demonstrates the efficacy of integrating machine learning and generative models to produce realistic and comprehensive synthetic precipitation-flood events for producing flood probability maps. The synthetic flood probability maps generated in this research provide valuable insights for urban planners, emergency management professionals, and policymakers, enabling more effective flood preparedness and mitigation strategies. This work represents a significant step forward in flood risk management, offering a scalable and flexible solution to address the

limitations of current flood risk mapping and characterization approaches. This study also contributes to efforts to expand simulated (synthetic) data for AI model development for disaster resilience use cases. Both real and synthetic (simulated) data are crucial for the development of robust AI models for various disaster resilience use cases ranging from risk prediction to situational awareness and impact assessment. Future studies can leverage GAN and other generative ML methods for augmenting limited real disaster datasets and produce datasets suitable for training and testing novel ML models for various disaster resilience applications.

## Acknowledgements

The authors would like to acknowledge funding support from the National Science Foundation under CRISP 2.0 Type 2, grant 1832662, and the Texas A&M X-Grant Presidential Excellence Fund. Any opinions, findings, conclusions, or recommendations expressed in this research are those of the authors and do not necessarily reflect the view of the funding agencies.

## Data Availability

The data that support the findings of this study is available from the corresponding author upon request.

## Code Availability

The code that supports the findings of this study is available from the corresponding author upon request.

## References

- [1] Enes Yildirim, Craig Just, and Ibrahim Demir. Flood risk assessment and quantification at the community and property level in the state of iowa. *International journal of disaster risk reduction*, 77:103106, 2022.
- [2] Keith N Musselman, Flavio Lehner, Kyoko Ikeda, Martyn P Clark, Andreas F Prein,anghai Liu, Mike Barlage, and Roy Rasmussen. Projected increases and shifts in rain-on-snow flood risk over western north america. *Nature Climate Change*, 8(9):808–812, 2018.
- [3] Louise J Slater and Gabriele Villarini. Recent trends in us flood risk. *Geophysical Research Letters*, 43(24):12–428, 2016.
- [4] Hong Kang Ji, Majid Mirzaei, Sai Hin Lai, Adnan Dehghani, and Amin Dehghani. Implementing generative adversarial network (gan) as a data-driven multi-site stochastic weather generator for flood frequency estimation. *Environmental Modelling & Software*, 172:105896, 2024.
- [5] Farzad Piadeh, Kourosh Behzadian, Albert S. Chen, Luiza C. Campos, Joseph P. Rizzuto, and Zoran Kapelan. Event-based decision support algorithm for real-time flood forecasting in urban drainage systems using machine learning modelling. *Environmental Modelling & Software*, 167:105772, 2023.
- [6] Saeed Saviz Naeini and Reda Snaiki. A physics-informed machine learning model for time-dependent wave runup prediction. *Ocean Engineering*, 295:116986, 2024.
- [7] Kaili Zhu, Chengguang Lai, Zhaoli Wang, Zhaoyang Zeng, Zhonghao Mao, and Xiaohong Chen. A novel framework for feature simplification and selection in flood susceptibility assessment based on machine learning. *Journal of Hydrology: Regional Studies*, 52:101739, 2024.
- [8] Hai-Min Lyu and Zhen-Yu Yin. Flood susceptibility prediction using tree-based machine learning models in the gba. *Sustainable Cities and Society*, 97:104744, 2023.
- [9] Diana McSpadden, Steven Goldenberg, Binata Roy, Malachi Schram, Jonathan L. Goodall, and Heather Richter. A comparison of machine learning surrogate models of street-scale flooding in norfolk, virginia. *Machine Learning with Applications*, 15:100518, 2024.
- [10] Cesar A.F. do Lago, Marcio H. Giacomoni, Roberto Bentivoglio, Riccardo Taormina, Marcus N. Gomes, and Eduardo M. Mendiondo. Generalizing rapid flood predictions to unseen urban catchments with conditional generative adversarial networks. *Journal of Hydrology*, 618:129276, 2023.
- [11] Jon Dewitz. National Land Cover Database (NLCD) 2019 Products, 2021.
- [12] 'USDA NRCS'. Gridded Soil Survey Geographic (gSSURGO) Database for the Conterminous United States, 2023.

- [13] 'Harris County Flood Control District'. Harris County Flood Warning System, 2023.
- [14] M. Garcia, A. Juan, J. Doss-Gollin, and P. Bedient. Leveraging mesh modularization to lower the computational cost of localized updates to regional 2D hydrodynamic model outputs. *Engineering Applications of Computational Fluid Mechanics*, 17(1):2225584, December 2023.
- [15] Markus Konrad. geovoronoi, February 2021.
- [16] Tianqi Chen and Carlos Guestrin. Xgboost: A scalable tree boosting system. In *Proceedings of the 22nd ACM SIGKDD international conference on knowledge discovery and data mining*, pages 785–794, 2016.
- [17] Ali Shehadeh, Odey Alshboul, Rabia Emhamed Al Mamlook, and Ola Hamedat. Machine learning models for predicting the residual value of heavy construction equipment: An evaluation of modified decision tree, lightgbm, and xgboost regression. *Automation in Construction*, 129:103827, 2021.
- [18] Ashish Vaswani, Noam Shazeer, Niki Parmar, Jakob Uszkoreit, Llion Jones, Aidan N Gomez, Łukasz Kaiser, and Illia Polosukhin. Attention is all you need. *Advances in neural information processing systems*, 30, 2017.
- [19] Marco Castangia, Lina Maria Medina Grajales, Alessandro Aliberti, Claudio Rossi, Alberto Macii, Enrico Macii, and Edoardo Patti. Transformer neural networks for interpretable flood forecasting. *Environmental Modelling & Software*, 160:105581, 2023.
- [20] Cheng-Chun Lee, Lipai Huang, Federico Antolini, Matthew Garcia, Andrew Juan, Samuel D Brody, and Ali Mostafavi. Predicting peak inundation depths with a physics informed machine learning model. *Scientific Reports*, 14(1):14826, 2024.
- [21] Davide Chicco, Matthijs J Warrens, and Giuseppe Jurman. The coefficient of determination r-squared is more informative than smape, mae, mape, mse and rmse in regression analysis evaluation. *PeerJ computer science*, 7:e623, 2021.
- [22] Neha Patki, Roy Wedge, and Kalyan Veeramachaneni. The synthetic data vault. In *IEEE International Conference on Data Science and Advanced Analytics (DSAA)*, pages 399–410, Oct 2016.
- [23] Lei Xu, Maria Skoularidou, Alfredo Cuesta-Infante, and Kalyan Veeramachaneni. Modeling tabular data using conditional gan. In *Advances in Neural Information Processing Systems*, 2019.
- [24] Marco Monge. Two-sample kolmogorov-smirnov tests as causality tests. a narrative of latin american inflation from 2020 to 2022. *Revista Chilena de Economía y Sociedad*, 2023.
- [25] Shichao Zhang. Nearest neighbor selection for iteratively knn imputation. *Journal of Systems and Software*, 85(11):2541–2552, 2012.
- [26] Florian Wagner, Yun Yan, and Itai Yanai. K-nearest neighbor smoothing for high-throughput single-cell rna-seq data. *BioRxiv*, page 217737, 2017.
- [27] MK Vijaymeena and K Kavitha. A survey on similarity measures in text mining. *Machine Learning and Applications: An International Journal*, 3(2):19–28, 2016.
- [28] David Freedman, Robert Pisani, and Roger Purves. Statistics (international student edition). *Pisani, R. Purves, 4th edn. WW Norton & Company, New York*, 2007.
- [29] John R Hershey and Peder A Olsen. Approximating the kullback leibler divergence between gaussian mixture models. In *2007 IEEE International Conference on Acoustics, Speech and Signal Processing-ICASSP'07*, volume 4, pages IV–317. IEEE, 2007.